Title:
Personalized Human Body Model Generation, Including Skeleton Utilizing 3D Body Scanning, Mesh Morphing, and Statistical Shape Modeling

Authors:
Satoshi Kanai, kanai@ssi.ist.hokudai.ac.jp, Hokkaido University
Ayane Sotome, a.sotome5@gmail.com, Formerly at Hokkaido University
Yui Endo, y.endo@aist.go.jp, National Institute of Advanced Industrial Science and Technology
Hiroaki Date, hdate@ssi.ist.hokudai.ac.jp, Hokkaido University

Keywords:
Digital Human, Mesh Morphing, Statistical Shape Model, 3D Scan, Radial Basis Function, Personalization

DOI: 10.14733/cadconfP.2024.243-248

Introduction:
Personalized human body models (PHBMs), designed to reflect individual physical characteristics, can significantly increase the effectiveness of training programs in sports and rehabilitation, as well as improve ergonomic evaluations [2]. The precise creation of a PHBM for musculoskeletal simulations demands that it accurately reflects an individual's organ and skeletal shapes, masses, and center of gravity derived from detailed body measurements. However, generating a PHBM through computed tomography (CT) or magnetic resonance imaging is time-consuming and costly, and it encounters medical constraints.

This study proposes a method to generate a PHBM with reasonable accuracy using only optical three-dimensional (3D) body scans. Initially, a reference body mesh, including skin, organs, muscles, and skeleton reconstructed from a CT scan, is prepared. This mesh is then smoothly deformed through mesh morphing techniques to conform to an individual skin model obtained from a 3D body scan. Afterward, adjustments are made to the internal pelvis shape using a statistical shape model. Finally, the inner organs and muscles are re-shaped to align with the individual skin and internal pelvis shape. The proposed PHBM's effectiveness is verified by applying personalized musculoskeletal simulations.

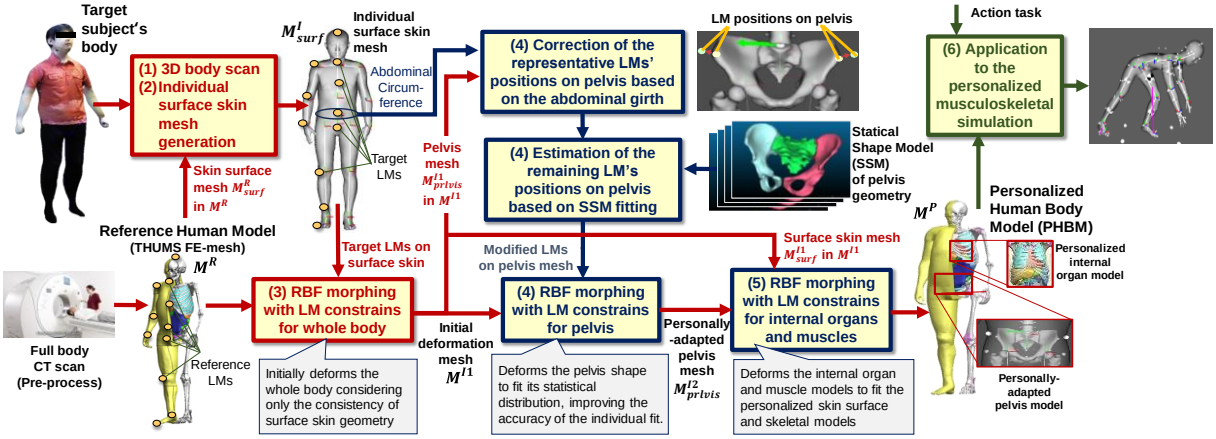

Fig. 1: Proposed personalized human body model generation workflow.

Overview of the Personalized Human Body Model (PHBM) Generation:

Fig. 1. outlines our PHBM generation flow, with the processing steps outlined below. To generate the PHBM, a male standing finite-element mesh of THUMS [5] was used as a reference human model M^R including surface skin, skeleton, internal organs, and muscles.

(1) The target subject's body is scanned using an optical 3D body scanner to generate a measured individual skin point cloud P^I_{surf}.
(2) Through deformation transfer [4], from P^I_{surf}, an individual skin surface mesh M^I_{surf} is generated that is homologous to the surface skin mesh M^R_{surf} of M^R, with anatomical landmarks (LMs) on the skin matching those on M^R_{surf}.
(3) The surface skin M^R_{surf} and skeleton M^R_{skel} meshes in M^R are smoothly deformed to generate an initial deformation mesh M^{I1} using radial basis function (RBF) mesh morphing [1] with the landmark (LM) constraints. This ensures that the LMs on M^R_{surf} are transformed to align with those on M^I_{surf}. This process results in an initial deformation of the whole body, considering only the consistency of the surface skin shape.
(4) The pelvis mesh M^{I1}_{pelvis} within the skeleton mesh M^{I1}_{skel} included in M^{I1} often exhibits significant fitting errors to the subject's pelvis. Thus, the shape of M^{I1}_{pelvis} is modified to generate a personally adapted pelvis mesh M^{I2}_{pelvis}. The modification uses a statistical shape model (SSM) of the pelvis, which we constructed from the statistical analysis of numerous pelvic CT measurements [3].
(5) The point clouds on the personalized surface skin mesh M^{I1}_{surf} and skeleton mesh M^{I2}_{skel} are set as the target LMs. Consequently, all elements, including internal organs and muscles, undergo further re-deformation through LM-constrained RBF mesh morphing to generate a PHBM M^P.
(6) Finally, to demonstrate the effectiveness of PHBM M^P, the model is applied to personalized musculoskeletal simulations. The mass distribution of each body part of M^P is reflected in the link model of the subject, and the outcomes are compared with the experimental results.

Landmark-Constrained RBF Mesh Morphing of Body Meshes:

The study employed LM-constrained RBF mesh morphing to smoothly deform the mesh model in processes (3), (4), and (5) as outlined above. The basic concept of RBF morphing is explained below, using process (3) as an illustrative example.

A deformation of a reference human model M^R is performed to ensure the LMs L^R_{surf} on M^R match the target LMs L^I_{surf} on M^I_{surf}. Through RBF mesh morphing [1] with LM constraints, the displacement $\boldsymbol{d}_i$ at each vertex $\boldsymbol{p}^R_i$ on M^R is determined. The mesh vertex position $\boldsymbol{p}^{I1}_i$ after deformation is calculated as $\boldsymbol{p}^{I1}_i = \boldsymbol{p}^R_i + \boldsymbol{d}_i$. When an $l \in \{x, y, z\}$ component of the displacement $\boldsymbol{d}(\in R^3)$ is expressed by $d_l(\boldsymbol{x})$ at an arbitrary position $\boldsymbol{x}(\in R^3)$, the RBF interpolation of $d_l(\boldsymbol{x})$ is defined by Eqn. (1):

$$d_l(\boldsymbol{x}) = p_l(\boldsymbol{x}) + \sum_{k=1}^{n} \lambda_{k,l}\, \varphi(\|\boldsymbol{x} - \boldsymbol{x}_k\|)\ ,\quad l \in \{x, y, z\} \tag{1}$$

where $\boldsymbol{x}_k (k = 1, .., n)$ is an LM position whose displacement is given, n represents the total number of LMs, $p_l(\boldsymbol{x})$ signifies a linear polynomial of $\boldsymbol{x}$ such that $p_l(\boldsymbol{x}) = [1 \ \ \boldsymbol{x}] \left[c_{l,1}, c_{l,2}, c_{l,3}, c_{l,4}\right]^t = [1 \ \ \boldsymbol{x}]\boldsymbol{C}_l$, $\lambda_{k,l}$ is a weight coefficient at $\boldsymbol{x}_k$, and $\varphi(\,)$ indicates a radial basis function of Gaussian form.

Let $\boldsymbol{q}_i = \left[q_{ix}, q_{iy}, q_{iz}\right] \in L^R_{surf}$ be a reference LM position and $\boldsymbol{r}_i = \left[r_{ix}, r_{iy}, r_{iz}\right] \in L^I_{surf}$ be a target LM position. The simultaneous Eqn. (2) is obtained with respect to $\lambda_{k,l}$ and $\boldsymbol{C}_l$ of $p_l(\boldsymbol{x})$, which satisfies the LM constraint.

$$\begin{bmatrix} A & B \\ B^t & \boldsymbol{0} \end{bmatrix} \begin{bmatrix} \boldsymbol{\lambda}_l \\ \boldsymbol{C}_l \end{bmatrix} = \begin{bmatrix} T_l \\ \boldsymbol{0} \end{bmatrix}, \quad l \in \{x, y, z\} \tag{2}$$

where, $B = \begin{bmatrix} 1 & \boldsymbol{q}_1 \\ \vdots & \vdots \\ 1 & \boldsymbol{q}_n \end{bmatrix}$, $T_l = \begin{bmatrix} r_{1l} - q_{1l} \\ \vdots \\ r_{nl} - q_{nl} \end{bmatrix}$, $\boldsymbol{\lambda}_l = \begin{bmatrix} \lambda_{1,l} \\ \vdots \\ \lambda_{n,l} \end{bmatrix}$, $A = [a_{ik}]$, and $a_{ik} = \varphi(\|\boldsymbol{q}_i - \boldsymbol{q}_k\|)$. Using $\boldsymbol{\lambda}_l$ and $\boldsymbol{C}_l$, the solutions of Eqn.(2), and assuming the number of vertices N on the reference mesh M^R, the displacement vector $\boldsymbol{d}_i = \left[d_{ix}, d_{iy}, d_{iz}\right]$ of the morphing that satisfies the constraint at the vertex $\boldsymbol{p}^R_i$ is obtained by Eqn. (3).

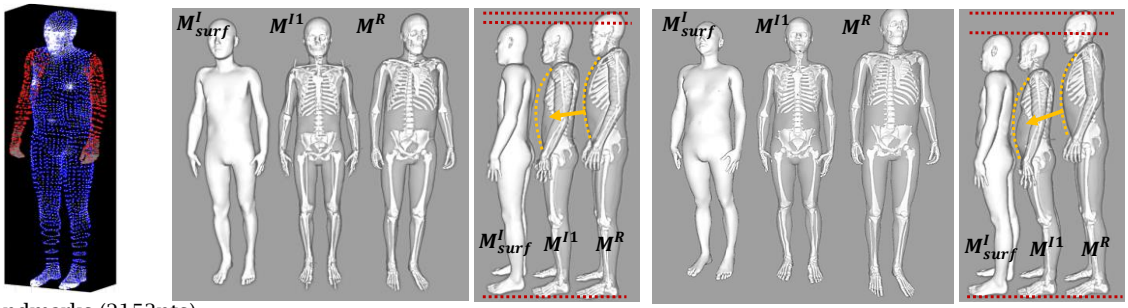

(a) Landmarks (2153pts) on torso (blue) and arms (red) on M^I_{surf}

(b) Mesh morphing result of a subject (173cm, BMI: 20.7) close to the height of M^R

(c) Mesh morphing result of a subject shorter (167cm, BMI: 21.7) than the height of M^R

Fig. 2: Initial deformation models using the landmark-constrained RBF mesh morphing.

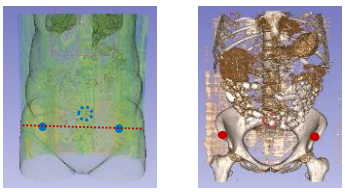

(a) Epidermal thickness measurement positions on abdominal CT data (Blue: Epidermis LM, Red: Pelvis LM)

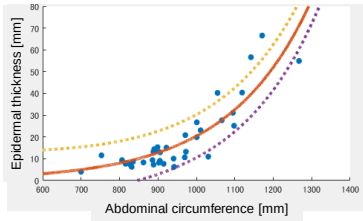

(b) Correlation between abdominal circumference and epidermal thickness (Male @ left and right superior anterior iliac spines)

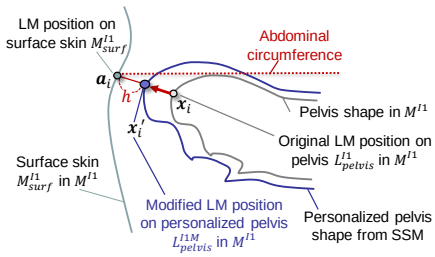

(c) Modification of LM position on pelvis

Fig. 3: Correction of the landmark positions on the pelvis.

$$T_l' = A'\,\boldsymbol{\lambda}_l + B'\boldsymbol{C}_l\,,\ l \in \{x, y, z\} \tag{3}$$

where $T_l' = [d_{1l}, \ldots\ldots, d_{Nl}]^t$, $A' = [a'_{ik}]$, $a'_{ik} = \varphi\left(\left\|\boldsymbol{p}_i^R - \boldsymbol{q}_k\right\|\right)$, $B' = \begin{bmatrix} 1 & \boldsymbol{p}_1^R \\ \vdots & \vdots \\ 1 & \boldsymbol{p}_N^R \end{bmatrix}$, $(i = 1, .., N)$, and $(k = 1, .., n)$.

From T_l' of Eqn. (3), all vertex positions of an initial deformation mesh M^{I1} homologous to M^R can be determined.

Fig. 2. shows an example of LMs L^I_{surf} on an individual skin mesh M^I_{surf}, and the RBF mesh morphing results for two subjects. The subjects were scanned using a noncontact 3D scanner. Fig. 2(b) and (c). display the initial deformation meshes M^{I1} generated by deforming M^R through RBF morphing. The whole body was smoothly deformed, with the subject's skeleton almost perfectly conforming to its body. The chest and abdomen of M^{I1} were also deformed appropriately for the individual surface skin shape. The deformation took 100 seconds.

Personal Adaptation of Pelvis Shape using Statistical Shape Model (SSM):

Correction of the Landmark Positions on Pelvis based on Abdominal Circumference

The RBF mesh morphing in the process (3) adapts M^R to M^I_{surf} solely based on the correspondence between LMs on the surface skins of both models. However, this approach does not account for individual differences in epidermal thickness near the superior anterior iliac spine and sacrum of the pelvis. Consequently, the estimation error in the pelvis LM position L^{I1}_{pelvis} in M^{I1} was deemed unacceptable.

We performed a regression analysis leveraging data from 37 lower abdominal CT scans to explore the relationship between epidermal thickness and abdominal circumference, aiming to reduce the estimation error [3]. As demonstrated in Fig. 3(a)., we measured epidermal thicknesses at three sites, namely the distances between the epidermal LMs and the pelvis LMs corresponding to the superior anterior iliac spines and sacral buttocks. Additionally, abdominal circumference was measured using a

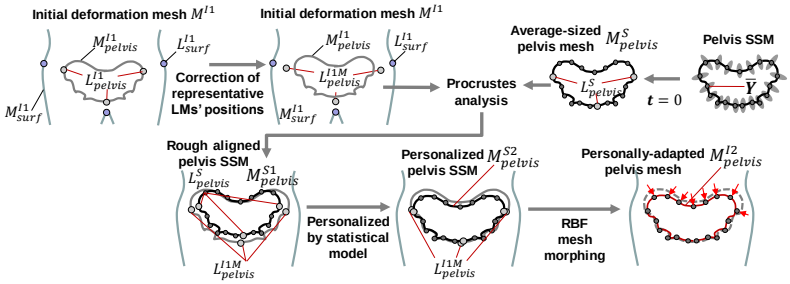

Fig. 4: Personal adaptation process of the pelvis mesh.

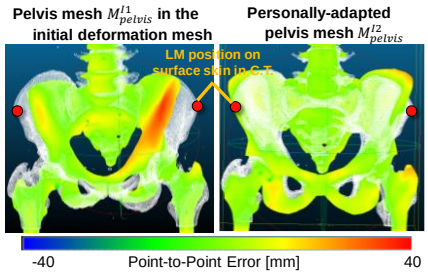

Fig. 5: Difference in errors between pelvis meshes (White dot: C.T. data).

transverse image capturing the epidermal LM. Fig. 3(b). shows that an exponential regression was applied to model the relationship between epidermal thickness and abdominal circumference. Based on this, Fig. 3(c). depicts how the three representative pelvis LMs' positions L^{I1}_{pelvis} in M^{I1} were adjusted to their corrected positions L^{I1M}_{pelvis} by changing the distance from the epidermal LM to the pelvis LM according to the epidermal thickness, assuming that the direction from the epidermal to the pelvis LMs was accurate.

Personal Adaptation of Pelvis Mesh using SSM and RBF Mesh Morphing

Among the primary skeleton structures (spine, pelvis, and ribcage), the spine and ribcage part M^{I}_{spine} in the initial deformation, mesh M^{I1} can be integrated into the PHBM since LMs on the skin are evenly distributed around the spine. However, the number of LMs that can define the pelvis position is relatively small, leading to potentially significant errors in estimating the skeleton geometry, even when the LM-constrained morphing is performed using only the three modified representative LMs on the pelvis L^{I1M}_{pelvis}.

To solve the issue, we first created an SSM [6] of the pelvis using abdominal CT data [3]. We then adapted the SSM size to fit an individual by using it as a new target for LMs during the morphing of the pelvis meshes M^{I1}_{pelvis} in M^{I1}, resulting in a personally adapted pelvis mesh M^{I2}_{pelvis}. The SSM can generate pelvis shapes of various sizes by changing the principal component scores according to Eqn. (4):

$$\boldsymbol{Y} = \bar{\boldsymbol{Y}} + F\boldsymbol{t} \tag{4}$$

where, $\boldsymbol{Y} = [\boldsymbol{y}_1, \boldsymbol{y}_2, \dots, \boldsymbol{y}_M]^t$, $\bar{\boldsymbol{Y}} = [\bar{\boldsymbol{y}}_1, \bar{\boldsymbol{y}}_2, \dots, \bar{\boldsymbol{y}}_M]^t$, $F = [\boldsymbol{f}_{ij}]$, $\boldsymbol{t} = [t_1, t_2, \dots, t_m]^t$, $\boldsymbol{y}_i (\in R^3)$ are the coordinates of the vertex i of SSM; $\bar{\boldsymbol{y}}_i (\in R^3)$ is the coordinate of the vertex i in the average size model; $\boldsymbol{f}_{ij} (\in R^3)$ is the basis vector quantifying the effect of jth principal component score on the coordinate of the vertex i; t_j is the principal component score; M is the number of SSM vertices; and $m (\ll M)$ is the number of valid principal components.

As shown in Fig. 4., the adaptation process of the pelvis SSM shape to an individual is performed as follows. From the pelvis SSM, we first generated an average-sized pelvis mesh M^{S}_{pelvis}. Subsequently, we identified and modified the representative LM positions on a pelvis closest to the LMs on M^{I}_{surf}, labeled as L^{S}_{pelvis} and L^{I1M}_{pelvis}, from the meshes M^{S}_{pelvis} and M^{I1}_{pelvis}, respectively. Using L^{S}_{pelvis} and the corresponding LMs L^{I1M}_{pelvis}, we performed a best-fit rigid transformation through Procrustes analysis, generating an average-sized statistical model M^{S1}_{pelvis} that aligns optimally with M^{I1}. Following this, we applied SSM deformation using Eqn. (5) to align the LM positions of L^{S1}_{pelvis} on M^{S1}_{pelvis} with the target LMs L^{I1M}_{pelvis}, resulting in a personalized pelvis SSM M^{S2}_{pelvis}:

$$\boldsymbol{Y}^* = \bar{\boldsymbol{Y}} + F F_L^{-} (\boldsymbol{Y}_L - \bar{\boldsymbol{Y}}_L) \tag{5}$$

where $\boldsymbol{Y}^*$ is the SSM vertex position after the deformation, $\boldsymbol{Y}_L$ is the LM position in L^{I1M}_{pelvis}, $\bar{\boldsymbol{Y}}_L$ is the LM position in L^{S1}_{pelvis} corresponding to $\boldsymbol{Y}_L$, and F_L^{-} is the generalized inverse matrix of the submatrix F_L extracted from F. Finally, M^{I1}_{pelvis} underwent another RBF morphing session to ensure that the sampled vertices $\{u\}$ on M^{I1}_{pelvis} coincide with the vertices closest to $\{u\}$ on M^{S2}_{pelvis}. This deformation yielded a

personally adapted pelvis mesh M_{pelvis}^{I2}, maintaining the same topology as M_{pelvis}^{R} and accurately fitting

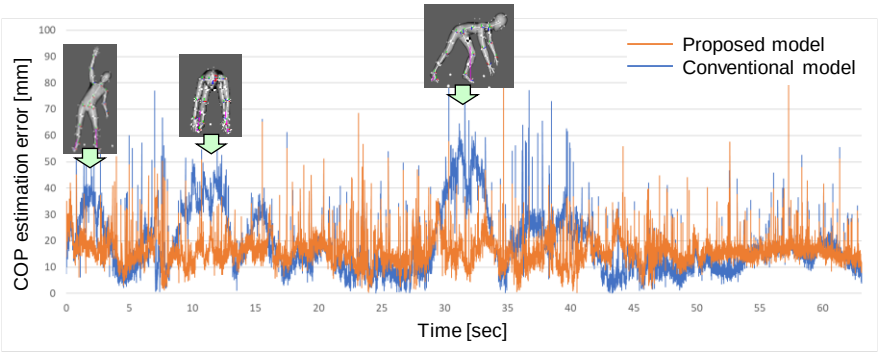

Fig. 6: Difference in COP estimation error between proposed and conventional models.

the subject's shape.

Fig. 5. shows the personally adapted pelvis models M_{pelvis}^{I2} for the subject shown in Fig. 2(b). Three LM positions on the pelvis were modified based on the epidermal thickness, which was estimated from the abdominal circumference, and the fitting of the pelvis SSM was performed using these LMs. Comparing the ground truth (GT) data of the subject with both the personalized mesh and the initial deformation mesh shown in Fig. 5., it is evident that the error in estimating the pelvis LMs at the superior anterior iliac spine in the PHBM has been reduced to 3 mm. This represents a significant improvement over the approximately 20 mm error observed in the initial deformation model. This demonstrates that the personally adapted pelvis mesh M_{pelvis}^{I2} can estimate a pelvis shape closer to the GT data.

Musculoskeletal Simulation with Personalized Human Body Model:

Finally, by using the mass distribution of each body part from the PHBMs fitted to a specific subject, we generated a mass-link model for musculoskeletal simulation, as shown in Fig. 6. The posture of each body part was measured through motion capture technology. We compared the center-of-gravity position (COP) error estimated by this mass-link model with the reference COP value obtained from a floor reaction force sensor. For comparison, we also evaluated the COP error derived from a link model that only fits the link dimensions commonly used in conventional musculoskeletal simulations and assumes a uniform mass distribution across the entire body. Fig. 6. compares the COP estimation errors between the proposed and conventional models during a 70-second exercise performed by a subject (male, 40 years old, height: 173 cm, BMI: 20.7). In some exercise intervals indicated in Fig. 6., where the COP variation is large, our proposed model succeeded in reducing the COP estimation error by about 20–30 mm more than the conventional model.

Conclusions:

To quickly generate a personalized human model from a reference human model based on a 3D body scan with consistent accuracy, we proposed a method that incorporates the personalized fitting of major skeletal and visceral models. This approach integrates body surface landmarks, SSMs, and mesh morphing techniques. Moreover, a mass-link model was generated for use in musculoskeletal simulations, and our findings indicated that this method significantly enhances simulation accuracy,

In future work, we will validate this method using GT data of a larger number of subjects and validate its effectiveness for individuals with significant body size variations compared to the reference model.

Satoshi Kanai, https://orcid.org/0000-0003-3570-1782
Ayane Sotome, http://orcid.org/0000-0001-8864-9995
Yui Endo, https://orcid.org/0000-0002-5541-5882
Hiroaki Date, https://orcid.org/0000-0002-6189-2044

References:

[1] Biancolini, M.-E.: Fast Radial Basis Functions for Engineering Applications, Springer Cham, 2017. https://doi.org/10.1007/978-3-319-75011-8

[2] Endo, Y.; Maruyama, T.; Tada, M.: DhaibaWorks: A software platform for human-centered cyber-physical systems, International Journal of Automation Technology, 17(3), 2023, 292-304. https://doi.org/10.20965/ijat.2023.p0292.

[3] Han, R.; Uneri, A.; De Silva, T.; Ketcha, M.; Goerres, J.; Vogt, S.; Kleinszig, G.; Osgood, G.; Siewerdsen, J.-H.: Atlas-based automatic planning and 3D-2D fluoroscopic guidance in pelvic trauma surgery, Physics in Medicine and Biology, 64(9), 2019, 095022. https://doi.org/10.1088/1361-6560/ab1456.

[4] Sumner, R.-W.; Popović J.: Deformation transfer for triangle meshes, ACM Transactions on Graphics, 23(3), 2004, 399-405. https://doi.org/10.1145/1015706.1015736

[5] THUMS, https://www.toyota.co.jp/thums, Toyota Motor Corporation.

[6] Verhaegen, F.; Meynen, A.; Matthews, H.; Claes, P.; Debeer, P.; Scheys, L.: Determination of pre-arthropathy scapular anatomy with a statistical shape model: part I—rotator cuff tear arthropathy, Journal of Shoulder and Elbow Surgery, 30(5), 2021, 1095-1106. https://doi.org/10.1016/j.jse.2020.07.043.